Chlorine activation and enhanced ozone depletion induced by wildfire aerosol

Susan Solomon[a,†#], Kane Stone[a,†], Pengfei Yu[b], D. M. Murphy[c], Doug Kinnison[d], A. R. Ravishankara[e], Peidong Wang[a]

[a]Department of Earth, Atmospheric, and Planetary Sciences, Massachusetts Institute of Technology, Cambridge, MA 02139

[b] Institute for Environmental and Climate Research, Jinan University, Guangzhou, China

[c]NOAA Chemical Sciences Laboratory, Boulder CO 80305

[d]Atmospheric Chemistry Observations and Modeling, National Center for Atmospheric Research, Boulder, CO 80307

[e]Departments of Chemistry and Atmospheric Science, Colorado State University, Fort Collins, CO 80523

†These authors contributed equally and are co first-authors of this work.

[#]corresponding author: solos@mit.edu

Accepted for publication in Nature

Remarkable perturbations in the stratospheric abundances of chlorine species and ozone were observed over southern hemisphere mid-latitudes following the 2020 Australian wildfires[1,2] . These changes in atmospheric chemical composition suggest that wildfire aerosols affect stratospheric chlorine and ozone depletion chemistry. Here we propose that wildfire aerosol containing a mixture of oxidized organics and sulfate[3-7] increases hydrochloric acid solubility[8-11] and associated heterogeneous reaction

rates, activating reactive chlorine species and enhancing ozone loss rates at relatively warm stratospheric temperatures. We test our hypothesis by comparing atmospheric observations to model simulations that include the proposed mechanism. Modelled changes in 2020 hydrochloric acid, chlorine nitrate, and hypochlorous acid abundances are in good agreement with observations[1,2]. Our results indicate that wildfire aerosol chemistry, while not accounting for the record duration of the 2020 Antarctic ozone hole, does yield an increase in its area, and a 3-5% depletion of southern mid-latitude total column ozone. These findings increase concern[2,12,13] that more frequent and intense wildfires could delay ozone recovery in a warming world.

Massive wildfires in Australia during austral summer of 2019-2020 (December-January) produced pyrocumulonimbus (pyroCb) towers that released about 0.9 Tg of wildfire smoke into the stratosphere[12,14]. Wildfires are also sometimes denoted as bushfires, wildland fires, and forest fires; here we refer to them as wildfires. Wildfire smoke can be expected to be primarily composed of organic material, but its stratospheric chemistry is virtually unknown.

Wildfire aerosol composition and aging

Airborne mass spectrometry data[15,16,17] showed that carbonaceous compounds were frequently present in about 30-40% of individual particles in the background northern hemisphere tropopause and lowermost stratosphere region. The

48 carbonaceous fraction was largely internally mixed with sulfate (i.e., both sulfate
49 and carbon were contained within single particles, although whether the latter
50 took the form of a coating was not determined). While the airborne instrument
51 was not flown through the Australian event, wildfire smoke of the Pacific
52 Northwest Event in 2017 displayed about a doubling of the carbonaceous/sulfate
53 aerosol population[17].
54
55 Aged stratospheric smoke particles can be characterized by thick coatings[18].
56 Infrared satellite spectra of the stratospheric wildfire smoke particles after the
57 2020 event revealed signatures of oxidized organic matter, in particular the OH
58 and C=O stretch features[2,19]. The smoke aerosols are referred to hereafter as
59 organic.
60
61 While the detailed composition of stratospheric smoke aerosols has not been
62 determined, tropospheric studies provide insights at lower altitudes. Fresh
63 tropospheric wildfire plumes contain a wide variety of complex organic
64 compounds including, for example, furans and phenolic compounds, and large
65 molecular weight species and humic-like substances can also be present[20].
66 Levoglucosan is a marker for biomass burning aerosols derived from the burning
67 of cellulose and hemicellulose, and is found in high concentrations in fresh
68 tropospheric plumes[21]. But levoglucosan is oxidized in particles by for example
69 reaction with OH, with a lifetime of about 1 day[22], and secondary aerosol
70 formation by other species is likely also important[23,24]. Here fresh smoke need

not be explicitly considered because we are interested in effects over timescales of weeks to months after the fires. The stratosphere is a highly oxidizing environment due to high concentrations of ozone and free radicals.

There is strong observational evidence for oxidation of many of the complex organic species seen in fresh plumes in the troposphere. Tropospheric observations reveal a variety of alcohols and acids in aged smoke particles. A wide range of organic acids were identified in tropospheric smoke from Portuguese wildfires including oleic acid (cis-9-octadecenoic acid), succinic acid, heptanedioic acid, malic acid, and oxo-acids, as well as several methoxyphenols and alcohols; n-alkanols from C_{10} to C_{30} and n-alkanoic acids from C_6 to C_{30} were also reported[6,24]. Oxalic acid is frequently among the most abundant single species found in aged tropospheric wildfire smoke aerosols[3-6,25,26]. It has been shown that organic acid content increased with smoke particle aging, and that carbohydrates such as levoglucosan are converted to organic acids during upward transport[3]. Aged aerosols from burning Australian vegetation have also been found to be hygroscopic and contain oxidized material[7], although whether eucalyptus burning might produce different specific organics than other vegetation types merits further study.

Whether stratospheric smoke is liquid, glassy, or solid must also be considered. Although the Australian plume had a depolarized lidar signature in the stratosphere which generally indicates solid particles, that was partly due to an unusual size

distribution as well as soot in the plume, and can still be consistent with a population of liquid-like particles[27,28,29]. A number of recent papers suggest that organic aerosols may form glasses[30-33]. However, complex mixtures of organics often take on liquid-like properties despite freezing or efflorescence behavior in the individual components[34,35]. Formation and maintenance of glasses can also be hindered by additional components (such as sulfate and nitrate) and for hygroscopic particles[36]. Following the formalism discussed in Methods, we estimate a diffuso-reactive length scale in organic liquid surfaces of the order of 0.01 microns at mid-latitudes and in polar autumn, driven in large part by the high liquid solubility (hence high particulate concentration) of HCl discussed below. The high HCl abundance in the particle implies that reaction is likely to occur very near the surface in particles of order a micron in size, and reduces the influence of diffusion on the reaction rate. Note that for stratospheric particles, ongoing rapid fluxes of water from/to the surface and the atmosphere as well as the presence of HCl often lead to a quasi-liquid layer, even for solid ice particles (e.g., ref. 37). We suggest that the stratospheric smoke particles likely started out deliquesced as they ascended in the humid environment of dense pyroCb clouds, then can be modelled as liquid-like at least for temperatures above about 195K; we further assume that stratospheric wildfire particles contain large amounts of oxidized organics, particularly organic acids, along with sulfate.

Modelling and testing wildfire chemistry

115 A sectional aerosol microphysics model (Community Aerosol and Radiation
116 Model for Atmospheres, CARMA) coupled with the Community Earth System
117 Model (CESM) has been shown to simulate both the observed sulfate and
118 organic/sulfate populations of background lower stratospheric particles.[38,39] This
119 model's application to the 2020 wildfires reproduced both the observed heating of
120 the stratosphere[12] and effects on NOx chemistry via the N_2O_5+H_2O
121 heterogeneous reaction[13]. Extended Data Fig. 1 shows that the calculated and
122 observed latitudinal and temporal spread of aerosol extinction during and after
123 the 2020 wildfires are in good general agreement at for example 18.5 km, see
124 also ref. 12. Here we use a specified dynamics version of this state-of-the-art
125 microphysics/atmospheric chemistry model (see Methods). The use of specified
126 dynamics based upon observations precludes study of dynamical or radiative
127 feedbacks but allows clear identification of chemical effects of different chemical
128 processes.
129
130 Most of the chlorine released from chlorofluorocarbons resides in HCl and
131 $ClONO_2$ in the lower stratosphere. The influence of organic/sulfate particles on
132 stratospheric chlorine chemistry (like that of background and volcanic aerosol
133 composed of sulfate/water particles, as well as Polar Stratospheric Clouds,
134 PSCs) can be expected to be linked to the dissolution and heterogeneous
135 reactions of these species[40]. The most important chlorine processing reactions
136 in/on stratospheric sulfate are
137

$$ClONO_2 + HCl \rightarrow Cl_2 + HNO_3 \quad (1)$$

$$ClONO_2 + H_2O \rightarrow HOCl + HNO_3 \quad (2)$$

$$HOCl + HCl \rightarrow Cl_2 + H_2O \quad (3)$$

$$HOBr + HCl \rightarrow BrCl + H_2O \quad (4)$$

The rates of these reactions in/on liquid sulfate particles are heavily dependent on temperature and water vapor partial pressure, which control the acidity and hence the solubility of the reactants, particularly HCl[41]. They are most effective on PSCs in the cold polar region at temperatures below about 195K (see Fig. 1), where they take on water, and HCl solubility increases. The above heterogeneous reactions then can rapidly deplete HCl (and $ClONO_2$), generating ClO and Cl_2O_2 and leading to the Antarctic ozone hole. The observed large 2020 mid-latitude decrease in HCl at much warmer mid-latitude temperatures suggests that HCl dissolution in mixed organic/sulfate smoke should be considered.

There is an extensive literature on HCl solubility in non-aqueous solvents dating to at least the 1930s[42], due to interest in basic physical chemistry questions such as the role of the dipole moment in the solubility process. Many more studies were published after the 1940s, in part linked to growth in industrial uses of HCl, for example in syntheses of various plastics and synthetic rubber. Illustrative examples of measured HCl solubility (mole fraction units)[8-11] versus temperature are presented in Fig. 1 for various types of oxidized organic compounds that may

be present in wildfire smoke; pure liquid water and liquid sulfate/water solutions are also shown for reference. The figure demonstrates that HCl is as (or more) soluble in many types of oxidized organics (ranging across alcohols, ethers, esters and acids) than in water at temperatures below about 260K; it is far more soluble in oxidized organics than in the background pure sulfate/water or PSC particles of the stratosphere unless temperatures fall below about 200K (e.g., in the Antarctic in winter and spring).

The reported solubility of HCl in formic acid (HCOOH) is lower than in the larger organic acids, but the higher molecular weight acids (C_3 and greater) show very similar values to one another, with increases at colder temperatures which approach those in the alcohols. The only organic acid for which solubility data below 220K are available in published literature is hexanoic acid. Since C_3 and larger oxidized organic acids are likely to be major components of aged stratospheric wildfire particles (as they are in the troposphere), here we adopt the solubility of HCl and its temperature dependence in hexanoic acid to approximately represent particulate oxidized organic matter in our numerical model calculations (see Methods). If, for example, more oxidized alcohols or ethers were present in the particles than acids, this would likely increase the HCl solubility slightly.

Because HCl is vastly more soluble in a wide variety of organics at temperatures above ≈200K than it is in background sulfate/water particles based on available

laboratory studies (Fig. 1), these data point towards a transformative role in mid-latitude stratospheric chemistry when oxidized organic aerosols are present in significant amounts. Although alternative elementary reactions are possible, an acid-catalyzed mechanism has been proposed[41,43] for reactions (1) and (2):

$HClONO_2^+$ *(liq)* + HCl *(liq)* → HNO_3 *(liq)* + Cl_2 *(liq, g)* + H^+ (5)

The high solubility of HCl in oxidized organics (Fig. 1) indicates that reaction (5) should occur readily at stratospheric temperatures. This process competes with reaction 2's first step:

$HClONO_2^+$*(liq)* + H_2O *(liq)* → HNO_3 *(liq)* + $H2OCl^+$ *(liq)* (6)

The high solubility of HCl in organic acids suggests that the available $HClONO_2^+$*(liq)* should be more likely to react with HCl *(liq)* than with H_2O *(liq)* in mixed organic/sulfate particles following this mechanism. This is consistent with the known reactivities of reactions (1) and (2) in liquid sulfate aerosols as HCl solubility and hence HCl *(liq)* concentrations increase at cold temperatures below about 195K, enhancing reaction (1) while suppressing (2); in contrast, reaction (2) is faster than (1) in sulfate particles at warmer temperatures[41]. Reactions (3) and (4) would also be enhanced by high concentrations of HCl (liq) and are included here.

To explore the influence of HCl solubility in wildfire particles, we carried out several tests. In one test, we use the HCl solubility in hexanoic acid data (hereafter referred to as solubility case) of Fig. 1 as approximately representative for the oxidized organic/sulfate particles (see Methods), which greatly increases the rates of reactions (1), (3), and (4) at warmer temperatures >200K. In a second test, we treat the liquid organic portion of the particles like water at all temperatures, i.e., we simply impose a dilution factor (dilution case) proportional to the organic content of the organic/sulfate/water particles. This alters the computed H_2SO_4 mole fraction and affects not only reactions (1), (3) and (4) but also (2). This could occur, for example, if the mechanism delineated in reactions (5) and (6) is not valid, enhancing the potential rate of the $ClONO_2$+H_2O reaction. In all wildfire model tests, smoke input changes the amount of total aerosol and its associated surface area, enhancing the N_2O_5+H_2O reaction rate; in a third test only that process is considered on the wildfire aerosols[13] in order to compare ozone depletion contributions from different processes (N_2O_5 only case). We compare these three tests to a control run that includes no organic particle chemistry (no organics case).

We find that the model calculated anomalies in chlorine species for the oxidized organics solubility case are in remarkable agreement overall with the unprecedented extreme changes seen in the 2020 southern mid-latitude observations (Fig. 2). Observed 2020 changes in ozone, HCl, $ClONO_2$, and ClO at 68 hPa relative to the climatological averages and ranges of available

observations for prior years from the Microwave Limb Sounder (MLS) and the Atmospheric Chemistry Experiment (ACE) satellite instruments are presented. Model results are 24-hour daily averages while observations shown are averages of available data (sunrise and sunset monthly averages for ACE; averages of daily day and nightside orbits for MLS). Corresponding absolute values for 2020 and the pre-2020 climatologies are shown in Extended Data Fig. 2. HOCl is also reported by ACE but is subject to greater uncertainty, and its anomalies and absolute concentrations are shown in Extended Data Fig. 3. The consistency between the model and measurements obtained across the various species, and over time during the year, strongly supports the proposed mechanism. Differences in absolute abundances likely largely reflect shortcomings in the transport processes of the model.

In contrast, the dilution case greatly overestimates the initial ClO (and HOCl) increases, and accordingly results in too much ozone loss (Fig. 2). In this case, reaction (2) is enhanced and then declines following the wildfire particle abundances. The fast rate of reaction (2) leads to reduced rather than enhanced autumn $ClONO_2$ as observed.

Taken together, these results suggest that atmospheric HCl indeed dissolves readily in smoke particles under stratospheric conditions, in a manner that is well captured by available solubility data in oxidized organics. This yields subsequent rapid reactions of HCl with $ClONO_2$ and HOCl and HOBr in the

253 particles at relatively warm mid-latitude temperatures, with reaction (1) being the
254 dominant process in the current model. Based upon the dilution case, it appears
255 that the $ClONO_2$+H_2O reaction is suppressed relative to the $ClONO_2$+HCl
256 reaction in these particles.
257
258 In contrast to HCl, satellite measurements indicate that stratospheric nitric acid
259 was not significantly perturbed by the Australian smoke[44], and the model is
260 consistent with those data (Extended Data Fig. 4). High values of $ClONO_2$ are
261 maintained in the sunlit atmosphere in the solubility case, limiting the potential for
262 ozone loss despite a rapid heterogeneous rate for reaction 1). This is due to
263 ongoing HNO_3 photolysis and reaction with OH, leading to reduced but non-zero
264 values of observed NO_2[40] and hence reformation of $ClONO_2$. Thus, a different
265 balance is obtained in mid-latitudes compared to the cold and dark polar regions,
266 where essentially no NO_2 is available to reform $ClONO_2$ after heterogeneous
267 loss, allowing far greater ClO anomalies to build up and form the ozone hole[40].
268 Nonetheless, $ClONO_2$ itself photolyzes rapidly and is approximately in
269 photochemical steady-state with ClO under sunlit mid-latitude conditions, so
270 increased $ClONO_2$ as seen in Fig. 2 implies that some increases in ClO and
271 ozone loss must occur. The shifts in chlorine chemistry result in a threefold
272 calculated increase in ClO, consistent with observations, and this leads to most
273 of the peak local ozone depletion of 10-20% during May to December as shown,
274 which is in accord with the record-low local ozone in this region in June according
275 to the data (Fig. 2). Extended Data Fig. 5 shows that the observed ozone loss

276 profiles on coincident days of observation are similar between ACE and MLS for
277 June-July as an example comparison.
278
279 Vertical anomaly profiles of HCl, ClO, and $ClONO_2$ averaged over all available
280 data and all model days for Jun-Jul, 2020 at southern midlatitudes are also fairly
281 well captured by the solubility case, albeit with some overestimates at higher
282 pressures (lower altitudes), further supporting the proposed mechanism through
283 its links to the profile of wildfire aerosols (Fig. 3). As in Fig. 2, the data do not
284 agree with the model dilution case. Corresponding absolute values are shown in
285 Extended Data Fig. 6.
286
287 The model suggests that the wildfire aerosols chemically deplete the mid-latitude
288 total ozone column from 30-50S by up to 18 DU, roughly triple the amount
289 obtained from N_2O_5 hydrolysis alone, yielding about 3-5% total chemical column
290 loss depending upon month of 2020. Such changes are relatively small
291 compared to the effects of interannual dynamical variability at mid-latitudes, and
292 there is evidence for some dynamically-driven decreases in ozone in 2020[1, 45].
293 Recent studies suggest that the radiative perturbations linked to wildfire smoke
294 affected 2020 southern hemisphere dynamical conditions and possibly ozone,
295 which could represent feedbacks in addition to the direct chemical effects
296 evaluated here[46, 47]. Nevertheless, the chemical changes are substantial in
297 comparison to the 1%/decade increase expected due to long-term decreases in
298 halocarbons that have occurred under the international Montreal Protocol, and

299 indicate that delays in ozone recovery could occur if wildfires become more
300 frequent or intense in the future.
301
302 Some studies have speculated that wildfires may deplete polar ozone[48]. The
303 Antarctic ozone hole of 2020 was both large in area and of record duration
304 (lasting through late December).[49] In sharp contrast with mid-latitudes, we find
305 that the observed polar 2020 abundances of ozone, HCl, ClONO2, and ClO for
306 68 hPa from 70-80°S show few marked departures from the ranges of past years
307 (Fig. 4). The small influence of our wildfire chemistry mechanism on ozone
308 losses in Antarctic spring can be expected because the adopted solubility of HCl
309 in organics becomes smaller than that of typical liquid PSCs below about 200K
310 (Fig. 1), i.e., in polar winter and spring when the ozone hole forms. Larger local
311 ozone changes are obtained close to the tropopause (i.e., 100-200 hPa, see
312 Extended Data Fig. 7) where temperatures are too warm for PSCs. However,
313 the concentration of ozone is relatively small at these altitudes, so the effect on
314 the polar total column depletion is modest (about 5% of the integrated column),
315 much less than that driven by PSCs at higher altitudes.
316
317 Importantly, observed 2020 polar HCl abundances in the austral autumn season
318 (April-May) decline far earlier (Fig. 4) than in any other year, and the model's
319 oxidized organics solubility case broadly reproduces this unusual behavior.
320 Temperatures at these latitudes and times are comparable to those in mid-
321 latitudes, so this is to be expected via the added chemistry. The observed HCl

inside the polar vortex is also effectively entirely removed by June-July in 2020, considerably lower than the no organics control case, or data in other years (Fig. 4 and maps in Extended Data Fig. 8).

A long-standing puzzle in stratospheric chemistry is that the observed timing of early winter HCl decline in the Antarctic and occasionally in the Arctic typically occurs earlier than models predict (see the comprehensive review in reference 50), as illustrated in Figs. 4 and Extended Data Fig. 8 for this model's no organics control case (similar to other models)[50]. Our simulations raise the question of whether early polar winter HCl declines could be linked to background levels of organic particles[15,16,17] in non-wildfire years.

While the early winter HCl discrepancy phenomenon is of long-standing chemical interest, our results provide further evidence that it causes limited changes in calculated Antarctic total column ozone depletion in this region[39]. Indeed, the control no-organics and organics runs both simulate the 70-80°S 2020 ozone losses and their record long duration well (Fig. 4), implying a dominant role for the observed unusually cold conditions in that year (as imposed based on a renalysis in these simulations). Inclusion of the wildfire organics HCl solubility does, however, expand the calculated area of the ozone hole (defined as the region where total column ozone is less than 220 Dobson Units) compared to the no organics control by about 2.5 million km^2 in September/October of 2020, contributing to the unusually large ozone hole in that year.

Wildfire aerosol in a warming world

Here we have shown that the effect of wildfire smoke on stratospheric chemistry consists not only of increases in particle surface area (as has been assumed in past literature)[12,13,45] but more importantly in profound impacts on HCl solubility and reactivity. In particular, the 2020 southern hemisphere mid-latitude lower stratospheric composition extremes in HCl, $ClONO_2$, ClO, HOCl are remarkably well reproduced by a model that considers the extremely high solubility of HCl in oxidized wildfire smoke organics at warm stratospheric temperatures (as indicated by historical laboratory solubility data) and subsequent reactions. These in turn deplete mid-latitude ozone.

A record-early observed 2020 southern autumn (April-May) disappearance of HCl at 70-80°S is another finding of this paper, and is well simulated by this model. Whether the smaller amounts of organic particles present in other years may be responsible for discrepancies between calculated and observed HCl declines[50] in high latitude autumn/winter documented in past literature merits future study.

While the model indicates that the organic particles expanded the size of the September/October 2020 ozone hole by about 2.5 million km^2, it does not explain its record longevity[49], raising the question of the roles of natural variability and

368 possible forcings (e.g., relation to the unusual mid-latitude ozone losses as well
369 as the radiative effects of the particles themselves and resulting impacts on
370 temperatures, winds, and stratosphere/troposphere coupling[46,47,49]). Further work
371 is needed to examine potential radiative and dynamical feedbacks of the aerosol
372 and ozone changes.
373
374 The same chemistry discussed here for the southern mid-latitudes and polar
375 regions can also be expected in northern hemisphere wildfire smoke. Further,
376 similar reactions should occur wherever aged organic aerosols and HCl are
377 found, i.e., not only in wildfire smoke but also in biomass burning, pollution, and
378 potentially aircraft-generated aerosols, both in the lower stratosphere and in the
379 troposphere. Consequences of HCl solubility in oxidized organics for long-term
380 lower stratospheric ozone trends also merit further study, along with potentially
381 altered solubilities of other compounds besides HCl in such particles in
382 tropospheric and stratospheric chemistry.
383
384 In closing, limitations of our chemical assumptions should be noted. For
385 example, it is possible that the organic material could freeze, even doing so at
386 warmer temperatures than normal, and thereby prolonging heterogeneous
387 chemistry in polar spring (and possibly autumn). Other reactions beyond those
388 considered may also be important, and new laboratory studies of solubility and
389 reactions of stratospheric species in oxidized organic aerosols and especially

wildfire aerosols are badly needed if, as expected, wildfire frequency and intensity increase in a warming world.

References

1. Santee, M. L. et al. Prolonged and pervasive perturbations in the composition of the Southern Hemisphere midlatitude lower stratosphere from the Australian New Year's fires. *Geophys. Res. Lett.* **49,** e2021GL096270 (2022).

2. Bernath, P., Boone, C., & Crouse, J. Wildfire smoke destroys stratospheric ozone, *Science* **375**, 1292–1295 (2022).

3. Gao, S., Hegg, D. A., Hobbs, P. V., Kirchstetter, T. W., Magi, B. I., & Sadilek, M. Water-soluble organic components in aerosols associated with savanna fires in Southern Africa: identification, evolution, and distribution. *J. Geophys. Res.* **108**, SAF 27-1 - SAF 21-16 (2003).

4. Kundu, S., Kawamura, K., Andreae, T.W., Hoffer, A. & Andreae, M.O. Molecular distributions of dicarboxylic acids, ketocarboxylic acids, and a-dicarbonyls in biomass burning aerosols: implications for photochemical production and degradation in smoke layer. *Atm. Chem. Phys*. **10**, 2209-2225 (2010).

5. Trebs, I., Meixner, F. Slanina, J., Otjes, R., Jongejan, P. & Andreae, M. O. Real-time measurements of ammonia, acidic trace gases and water-soluble inorganic aerosol species at a rural site in the Amazon Basin. *Atmos. Chem. Phys.* **4**, 967– 987 (2004).

6. Vicente, A., Alves, C., Monteiro, C., Nunes, T., Mirante, F., Cerqueira, M., Calvo, A., & Pio, C. Organic speciation of aerosols from wildfires in central Portugal during summer 2009. *Atmos. Env*. **57**, 186-196 (2012).

7. Mallet, M. D. et al. Composition, size and cloud condensation nuclei activity of biomass burning aerosol from northern Australian savannah fires. *Atm. Chem. Phys.* **17**, 3605-3617 (2017).

8. Ahmed, W., Gerrard, W., & Malukdar,V. K. Significance of the solubility of hydrogen halides in liquid compounds. *J. Appl. Chem.* **20**, 109-116 (1970).

9. Gerrard, W., & Macklen, E. Solubility of hydrogen halides in organic compounds containing oxygen. 1. Solubility of hydrogen chloride in alcohols, carboxylic acids, and esters, *J. Appl. Chem*. **6**, 241-244 (1956).

10. Gerrard, W., Mincer, A. M. A. & Wyvill, P. L. Solubiity of hydrogen halides in organic compounds containing oxygen III. Solubility of hydrogen chloride in alcohols and certain esters at low temperatures, *J. Appl. Chem*. **9**, 89-93, (1959).

11. International Union of Pure and Applied Chemistry (IUPAC), P. G. T. Fogg, P.G.T. & Gerrard, W., eds. *Solubility data series volume 42, Hydrogen halides in non-aqueous solvents*, Pergamon Press, ISBN 0-08-023925-0 (1990).

12. Yu, P. et al. Persistent stratospheric warming due to 2019-2020 Australian wildfire smoke. *Geophys. Res. Lett.* **48**, e2021GL092609 (2021).

13. Solomon, S. et al. On the stratospheric chemistry of midlatitude wildfire smoke. *Proc. Natl. Acad. Sci.* **119**, e2117325119 (2022).

14. Peterson, D. A. et al. Australia's Black Summer pyrocumulonimbus super outbreak reveals potential for increasingly extreme stratospheric smoke events. *npj Clim Atmo Sci*. **4**, 1-16 (2021).

15. Murphy, D. M., Thomson, D. S. & Mahoney, M. J. In situ measurements of organics, meteoritic material, mercury, and other elements in aerosols at 5 to 19 kilometers. *Science* **282**, 1664–1669 (1998).

16. Murphy, D. M., Cziczo, D. J., Hudson, P. K. & Thomson, D. S. Carbonaceous material in aerosol particles in the lower stratosphere and tropopause region. *J. Geophys. Res.* **112**, D04203 (2007).

17. Murphy, D. M. et al. Radiative and chemical implications of the size and composition of aerosol particles in the existing or modified global stratosphere. *Atmos. Chem. Phys.* **21**, 8915–8932 (2021).

18. Ditas, J, Ma, N., Zhang, Y., & Cheng, Y. Strong Impact of wildfires on the abundance and aging of black carbon in the lowermost stratosphere. *Proc. Natl. Acad. Sci.* **115**, E11595-E11603 (2018).

19. Boone, C. D., Bernath, P. F., & Fromm, M. D. Pyrocumulonimbus stratospheric plume injections measured by the ACE-FTS. *Geophys. Res. Lett.* **47**, e2020GL088442 (2020).

20. Palm, B. B., Peng, Q., Fredrickson, C. D. & Thornton, J. A. Quantification of organic aerosol and brown carbon evolution in fresh wildfire plumes, *Proc. Nat. Acad. Sci.* **117**, 29469–29477 (2020).

21. Sannigrahi, P., Sullivan, A. P., Weber, R. J. & Ingall, E. D. Characterization of water-soluble organic carbon in urban atmospheric aerosols using solid-state ^{13}C NMR spectroscopy. *Env. Sci. Tech.* 40, 3, 666–672 (2006).

22. Garofalo, L. A., Pothier, M. A., Levin, E. J. T., Campos, T., Kreidenweis, S. M. & Farmer, D. K. Emission and evolution of submicron organic aerosol in smoke from wildfires in the western United States, ACS Earth Space Chem., 3, 1237-1247 (2019).

23. Cappa, C. D., et al. Biomass-burning derived particles from a wide variety of fuels -Part 2: Effects of photochemical aging on particle optical and chemical properties. *Atm. Chem. Phys.* 20, 8511–8532 (2020).

24. Vicente, A., Alves, C., Calvo, A. I., Fernandes, A. P., Nunes, T., Monteiro, C., Almeida, S. M. & Pio, C. Emission factors and detailed chemical composition of smoke particles from the 2010 wildfire season. *Atmos. Env*., **71**, 295-303 (2013).

25. Mochida, M.,et al. Spatial distributions of oxygenated organic compounds (dicarboxylic acids, fatty acids, and levoglucosan) in marine aerosols over the western Pacific and off the coast of East Asia: Continental outflow of organic aerosols during the ACE-Asia campaign. *J. Geophys. Res*. **108**, 8638 (2003).

26. Deshmukh, D. K., et al. High loadings of water-soluble oxalic acid and related compounds in PM2.5 aerosols in eastern central India: Influence of biomass burning and photochemical processing. *Aerosol Air Qual. Res*. **19**, 2625-2644 (2019).

27. Haarig, M. et al., Depolarization and lidar ratios at 355, 532, and 1064 nm and microphysical properties of aged tropospheric and stratospheric Canadian wildfire smoke. *Atm. Chem. Phys*. **18**, 11847–11861 (2018).

28. Ohneiser, K. et al. Smoke of extreme Australian bushfires observed in the stratosphere over Punta Arenas, Chile in January 2020: optical thickness, lidar ratios, and depolarization ratios at 355 and 532 nm. *Atm. Chem. Phys*. **20**, 8003-8015 (2020).

487 29. Ansmann, A. et al. Tropospheric and stratospheric wildfire smoke profiling
488 with lidar: mass, surface area, CCN, and INP retrieval. *Atmos. Chem. Phys.*
489 **21**, 9779-9807 (2021).
490 30. Zobrist, B., Marcolli, C., Pedenera, D. A. & Koop, T. Do atmospheric
491 aerosols form glasses? *Atmos. Chem. Phys.* **8**, 5221-5244, 2008.
492 31. Virtanen, A., et al. An amorphous solid state of biogenic secondary organic
493 aerosol particles. *Nature* **467**, 824-827 (2010).
494 32. Reid, J. P. et al. The viscosity of atmospherically relevant organic particles.
495 *Nat. Comm.* **9**, 956 (2018).
496 33. Boomian, V., Creszenzo, G. V., Mahrt, F., Shirawa, M., Bertran, A. K. &
497 Nizkorodov, S. A. Sunlight can convert atmospheric aerosols into a glassy
498 solid state and modify their environmental impacts. *Proc. Nat. Acad. Sci.,*
499 **119**, (43) e2208121119 https://doi.org/10.1073/pnas.2208121119 (2022).
500
501 34. Cappa, C. D., Lovejoy, E.R. & Ravishankara, A. R. Evidence for liquid-like
502 and nonideal behavior of a mixture of organic aerosol components. *Proc. Nat.*
503 *Acad. Sci.* **105**,18687-18691 (2008).
504
505 35. Marcolli, C., Luo, B.P., & Peter, T. Mixing of the organic aerosol fractions:
506 Liquids as the thermodynamically stable phases. *J Phys Chem A* **108**, 2216–
507 2224 (2004).
508 36. Koop, T., Bookhold, J., Shirawa, M., & Poeschl, U. Glass transition and
509 phase state of organic compounds: dependency on molecular properties and

implications for secondary organic aerosols in the atmosphere. *Phys. Chem. Chem. Phys.* **13**, 19238‑19255 (2011).

37. McNeill, V. F., Loerting, T., Geiger, F. M., Trout, B. L. & Molina, M. J. Hydrogen chloride-induced surface disordering on ice. *Proc. Natl. Acad. Sci,* **103**, 9422-9427 (2006).

38. Yu, P. et al. Evaluations of tropospheric aerosol properties simulated by the community earth system model with a sectional aerosol microphysics scheme. *J. Adv. Model. Earth Syst.* **7**, 865-914 (2015).

39. Yu, P. et al. Radiative forcing from anthropogenic sulfur and organic emissions reaching the stratosphere. *Geophys. Res. Lett*., **43**, 9361–9367 (2016).

40. Solomon, S. Stratospheric ozone depletion: A review of concepts and history. *Rev. Geophys.* **37**, 275–316 (1999).

41. Shi, Q., Jayne, J. T., Kolb, C. E., Worsnop, D. R. & Davidovits, P. Kinetic model for reaction of $ClONO_2$ with H_2O and HCl and HOCl with HCl in sulfuric acid solutions. *J. Geophys. Res.* **106**, 24259–24274 (2001).

42. Bell, R. P., The electrical energy of dipole moments in solution, and the solubilities of ammonia, hydrogen chloride, and hydrogen sulfide, in various solvents. *J. Chem. Soc.* 1371-1382 https://doi.org/10.1039/JR9310001371 (1931).

531 43. Robinson, G. N., Worsnop, D. R., Jayne, J. T., Kolb, C. E. & Davidovits, P.
532 Heterogeneous uptake of $ClONO_2$ and N_2O_5 by sulfuric acid solutions. *J.*
533 *Geophys. Res.,* **102**, 3583-3601 (1997).

534 44. Schwartz M. J. *et al.* Australian New Year's pyroCb Impact on stratospheric
535 composition. *Geophys. Res. Lett.* **47,** e2020GL090831 (2020).
536
537 45. Strahan, S. E., et al. Unexpected repartitioning of stratospheric inorganic
538 chlorine after the 2020 Australian wildfires. *Geophys. Res. Lett* **49**,
539 e2022GL098290 (2022).
540 46. Yook, S., Thompson, D. W. J., & Solomon, S. Climate impacts and potential drivers
541 of the unprecedented Antarctic ozone holes of 2020 and 2021. *Geophys. Res. Lett.*
542 **49,** e2022GL098064. https://doi. org/10.1029/2022GL098064 (2022).
543 47. Damany-Pearce, *et al.* Australian wildfires cause the largest stratospheric warming
544 since Pinatubo and extends the lifetime of the Antarctic ozone hole. *Sci Rep* **12**,
545 12665 https://doi.org/10.1038/s41598-022-15794-3 (2022).

546 48. Ohneiser, K., et al. The unexpected smoke layer in the high Arctic winter
547 stratosphere during MOSAiC 2019-2020. *Atm. Chem. Phys*. **21**, 15783-157808
548 (2021).

549 49. Klekociuk, A.R. *et al.* The Antarctic ozone hole during 2020. *J. Southern*
550 *Hemisphere Earth Systems Science* **72**(1), 19–37 (2022).

50. J.-U. Grooß, *et al.* On the discrepancy of HCl processing in the core of the wintertime polar vortices. *Atmos. Chem. Phys.* **18**, 8647–8666 (2018).

Methods

Model simulations

We use the sectional aerosol model, Community Aerosol and Radiation Model for Atmospheres (CARMA) coupled with the NSF/DOE Community Earth System Model (CESM-CARMA)[38, 39, 51, 52]. We spin-up by running the model from a multi-year free running simulation, and continue in free-running mode from Dec.29, 2019 to Mar.1, 2020, which allows the initial injection to be self-lofted into the stratosphere, as shown in reference 12. We inject 0.9 Tg of smoke (3 times that of the Pacific Northwest fires in 2017) during the fire days of December 29–31 2019 and January 4 2020 over southeastern Australia (39°S, 150°E) at an altitude of 12 km[12]. The smoke is made up of 2.5% black carbon which is a factor in the lofting of the injected smoke; sensitivity simulations with other values in this model[12] show that this percentage gave the best match to satellite observations in this model. After March 1, simulated winds and temperature are nudged to the Goddard Earth Observing System version 5 analysis (GEOS-5)[53] to ensure accurate meteorological conditions for 2020 that are insensitive to the upper boundary, and optimize comparisons with observations.

574 The model includes 56 layers from the surface up to 1.8 hPa (about 45 km) with
575 a vertical resolution of about 1 km in the upper troposphere and lower
576 stratosphere. The horizontal resolution of the model is 1.9° latitude × 2.5°
577 longitude.
578
579 The model calculates two kinds of organic aerosols: 1) organic material mixed
580 with sulfate, black carbon, sea salt, and dust and 2) purely organic smoke
581 particles emitted from the fires. Both sets of particles are computed in 20 size
582 bins whose radii range from 0.05–8.7 μm. The model includes both the oxidation
583 of the organic component of the smoke by ozone and condensation of sulfuric
584 acid upon the smoke particles[12].
585
586 Stratospheric heterogeneous chemistry rates in and on aerosols are calculated
587 using the kinetics parameterization approach generally employed in atmospheric
588 chemistry models[41] for the heterogeneous reactions of $ClONO_2$ + HCl, $ClONO_2$ +
589 H2O, and HOCl +HCl. The kinetics approach uses experimental data for HCl,
590 HOCl, and $ClONO_2$ liquid diffusion, solubility, and reactivity to obtain the
591 heterogeneous reactions for H_2SO_4/H_2O stratospheric aerosol heterogeneous
592 kinetics.
593
594 To investigate the effect of smoke on stratospheric chemistry, 4 model setups are
595 used that adopt different heterogeneous chemistry on stratospheric aerosols.

Further detail on the oxidized organic HCl solubility and dilution cases (see Main text) are as follows:

Dilution. This simulation assumes the organic carbon behaves as an aerosol diluent and combines with the H_2SO_4/H_2O aerosols, which effectively lowers the H_2SO_4 weight percent that is a key parameter in the kinetics parameterization[41]. This is achieved by

$$wt_d = \frac{1}{1/wt + OC/SO_4}$$

Where wt is the weight percent of H_2SO_4 in the H_2SO_4/H_2O solution, wt_d is the diluted H_2SO_4 weight percent, OC is the organic carbon mass concentration, and SO_4 is the sulfur mass concentration. An estimate of the organic molar mass of 116 (hexanoic acid) is used to obtain the organic weight corrected H_2SO_4 mole fraction as follows

$$x_{h2so4} = \frac{wt_d}{wt_d + \frac{wt_{H_2O} \times 98}{18} + \frac{wt_{oc} \times 98}{116}}$$

which is then used in the calculation of HCl solubility. Here wt_{H2O}, and wt_{oc} are the weight percent of water and organic carbon, respectively, 98 is the molar mass of H_2SO_4, 18 is the molar mass of H_2O and 116 is the molar mass of hexanoic acid.

Solubility. This simulation alters the HCl solubility to account for the effects of smoke organics using laboratory measurements[8-11](instead of changing the H_2SO_4 weight percent). This is done for all locations and times when the ratio of mass concentration of organic carbon to sulfur is > 1; otherwise the original parameterization[41] is used. Following reference 11, the HCl mole fraction in hexanoic acid is calculated using the following fit function to the laboratory data points (see red diamonds in Fig. 1, where the red line through them indicates this fit):

$$x_{hcl} = \exp\left(28.99 - \frac{3300.46}{T} - 18.14 \times log\left(\frac{T}{100}\right)\right)$$

where T is the temperature. As hexanoic acid is a weak acid, we assume that HCl dissociates in hexanoic acid similarly to water. Mole fraction is converted to mole ratio (r_{hcl}), and used to calculate an effective Henry's law coefficient using a dissociation constant of HCl in water of $10^{5.9}$ (following reference 54)

$$H_{HCl} = \frac{r_{hcl} \times \rho_{hex} \times 10^{5.9}}{116}$$

where ρ_{hex} is given by[55]:

$$\rho_{hex} = (-5.01 \times 10^{-7} \times T^2 - 5.23 \times 10^{-4} \times T + 1.12) \times 1000$$

The rates of the heterogeneous reactions are then calculated in the kinetics parameterization[41] using this new value of Henry's law for HCl solubility in hexanoic acid. Because organic acids are weak acids, we assume that the acidity in a mixed organic/sulfuric acid solution would be determined largely by the sulfuric acid content. We do not consider the possible increase in pH due to interactions of these organics with sulfuric acid, and assume such changes to be small.

A caveat of this approach is that in principle the effective Henry's law best applies to dilute solutions so that some uncertainty occurs for strong solutions but laboratory data suggests this is a small effect for our purposes[8].

Observations

We use the MLS Level 2, version 5 PressureZM measurement product for O_3, HCl, HNO_3, and ClO data[56] in order to analyze mid-latitude (30–50°S) and polar (70–80°S) time series at 68 hPa as well as O_3 and ClO vertical profiles between 30–50°S. We use the Level 2, version 5 PressureGrid measurement product for HCl maps. MLS has the benefit of daily measurements with few data gaps, and allows for comprehensive temporal comparison with the model over all months in 2020. However, note that the ClO measurements at lower levels (68–147 hPa) are subject to a known negative bias. At 68 hPa the bias is relatively small and

has been reduced in version 5 compared to the previous version 4.2. It is therefore recommended[56] that day minus night measurements be used to reduce the bias. However, for the purposes of this paper where comparison with model weekly average output is required and absolute values are less important as opposed to anomalies, we opted to use the averages of MLS day and night data. This also has the additional benefit of not having to account for additional biases in the polar region for the MLS day minus night product.

In addition, we use the ACE-FTS version 4.1 data[57] for $ClONO_2$ and HOCl time series at 68 hPa and between 30–50°S for midlatitudes and 70°–80˚S for polar conditions. We also use ACE for vertical profiles of $ClONO_2$ and HCl during June and July between 30–50°S. Use of ACE HCl data here maximizes altitude coverage. ACE has sporadic spatial coverage for specific latitude ranges. Therefore, for the time series of $ClONO_2$, monthly averages of the available daily data for each month are constructed. For example, there is no data coverage between 30–50°S in May and September. ACE quality control is performed by removing data points that lie outside 3 standard deviations of the mean values as suggested for this data product[57].

ACE and model data are interpolated onto a regular grid which coincides with the MLS pressure grid product to allow for appropriate comparison between datasets.

Data Availability

All data used in this study is publicly available. MLS data: https://disc.gsfc.nasa.gov/datasets?page=1&source=Aura%20MLS; ACE-FTS data: http://www.ace.uwaterloo.ca (with registration: https://databace.scisat.ca/l2signup.php); CESM1-CARMA: https://doi.org/10.7910/DVN/GHNJQA.

Code Availability

The model used in this study can be accessed via https://www.cesm.ucar.edu/models/cesm1.2/cesm/doc/usersguide/x290.html.

The changes described herein for the kinetics parameterization are available at: https://doi.org/10.7910/DVN/GHNJQA.

51. Bardeen, C. G., Toon, O. B., Jensen, E. J., Marsh, D. R., & Harvey, V. L. Numerical simulations of the three-dimensional distribution of meteoric dust in the mesosphere and upper stratosphere. Journal of Geophysical Research, 113, D17202 (2008).

52. Toon, O. B., Turco, R. P., Westphal, D., Malone, R., & Liu, M. (1988). A multidimensional model for aerosols—Description of computational analogs. *J. Atm. Sci.*, **45**, 2123-2143 (1988).

53. Rienecker, M. M., et al. The GEOS-5 Data Assimilation System—Documentation of Versions 5.0.1 and 5.1.0. NASA GSFC Technical Report Series on Global Modeling and Data Assimilation, vol. **27**, pp. 92, *NASA/TM-2007-104606* (2008).

54. Trummal, A., Lipping, L., Kaljurand, I., Koppel I.A., Leito, I. Acidity of strong acids in water and dimethyl sulfoxide. *J. Phys. Chem. A* **120**, 3663–3669 (2016).

55. Ghatee, M. H., Ghanavati. F., Bahrami, M,, Zolghadr, A. R. Molecular dynamics simulation and experimental approach to the temperature dependent surface and bulk properties of hexanoic acid. *Ind. Eng. Chem. Res.* **52**, 3334–3341 (2013).

56. Livesey, N. J., Read, W. G., Wagner, P. A., Froidevaux, L., Santee, M. L., Schwartz, M. J., et al. Version 5.0x level 2 and 3 data quality and description document. (Tech. Rep. No. JPL D-105336 Rev. A). Jet Propulsion Laboratory, (2020). Retrieved from http://mls.jpl.nasa.gov

57. Boone, C. D., Bernath, P. F., Cok, D., Jones, S. C., & Steffen, J. Version 4 retrievals for the atmospheric chemistry experiment Fourier transform spectrometer (ACE-FTS) and imagers. *Journal of Quantitative Spectroscopy & Radiative Transfer*, 247, 106939 (2020).

Acknowledgements. SS and KS are partly supported by NSF 1848863. DEK was funded in part by NASA grant (80NSSC19K0952). PY is supported by the National Natural Science Foundation of China (42175089, 42121004). DM is supported by NOAA base and climate funding. The CESM project is supported by the National Science Foundation and the Office of Science (BER) of the U.S. Department of Energy. We gratefully acknowledge high-performance computing support from Cheyenne (doi:10.5065/D6RX99HX) provided by NCAR's

732 Computational and Information Systems Laboratory, sponsored by the National
733 Science Foundation.

734 **Author contributions** SS and KS contributed equally and are co first-authors of
735 this study**.** S.S., K. S., P.Yu, and D.M. designed the initial work. K. S. analyzed
736 the data and refined study design, and produced the figures. S.S. drafted the
737 initial text. K. S., D. M., D.K., A. R. R. and P.W contributed significantly to the
738 interpretation of findings and to the revisions of the manuscript.

739 **Competing interests** The authors declare no competing interests.

740 **Correspondence and requests for materials** should be addressed to Susan
741 Solomon (solos@mit.edu).

744 Figures

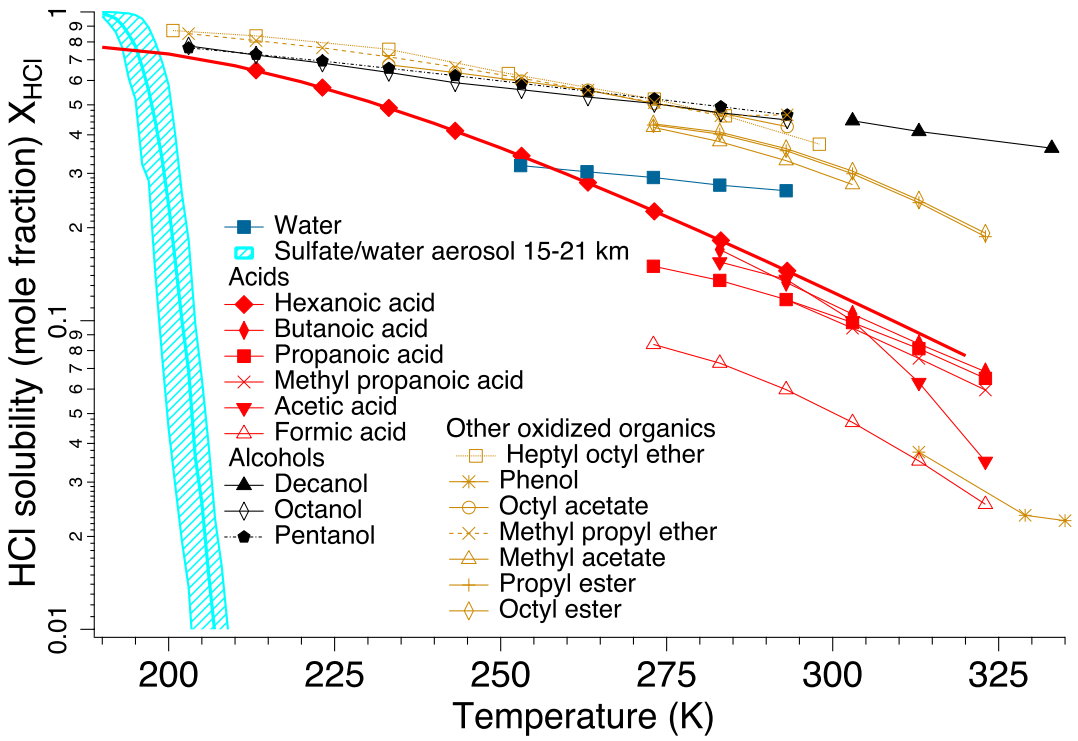

745

746 Fig. 1. **HCl solubility in different liquids.** Solubility (in mole fraction) of HCl in various
747 organics, pure water, and sulfate/water mixtures is shown as a function of temperature
748 based upon available laboratory data. The values shown for sulfate/water mixtures are
749 for typical stratospheric conditions over the height range from about 15 to 21 km and
750 are taken from the model used here.

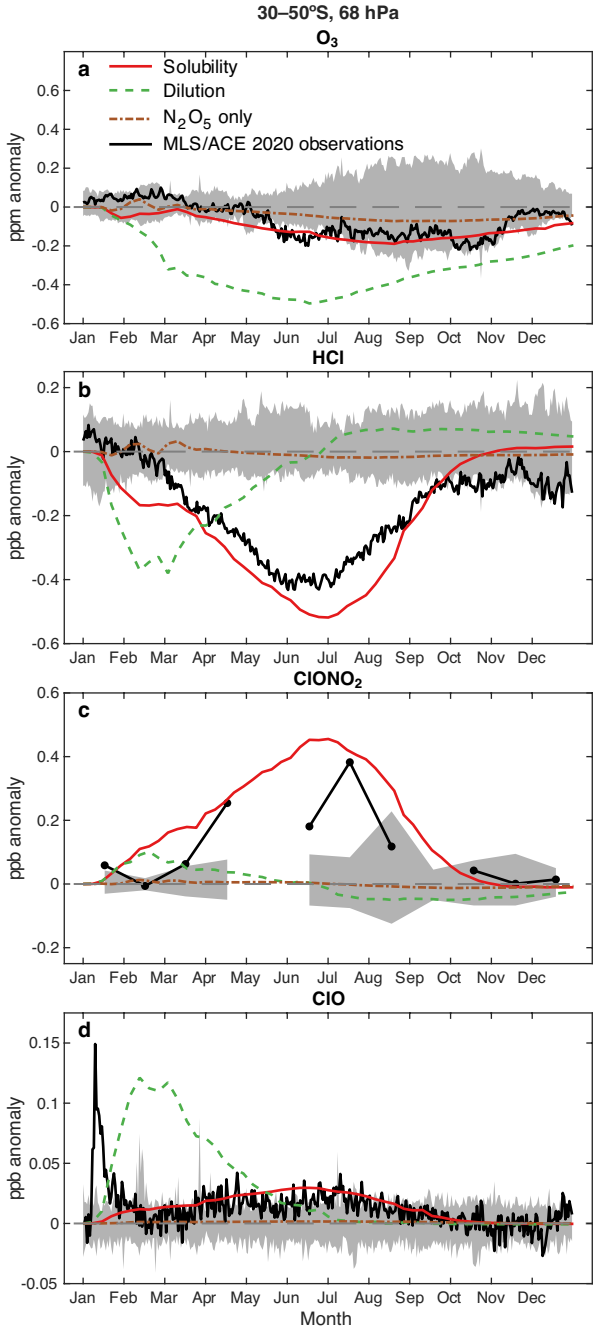

751

752 Fig. 2. **Observed and modelled 2020 anomalies in chemical species from 30-50°S at 68**

753 **hPa.** Gray shaded regions show the ranges of 24-hour averaged satellite data anomalies

754 relative to the climatologies of satellite observations prior to 2020 (daily O_3, HCl, and

755 ClO from MLS, and monthly $ClONO_2$ from ACE), while black lines show the observed

756 anomalies for 2020. Other colored lines denote calculated anomalies relative to the

757 modelled no organics control for three model test cases: including only N_2O_5 hydrolysis
758 on the aerosols (brown dashed line), considering the added organic material as a
759 dilution factor (green dashed line), and considering the adopted solubility of HCl in
760 organic particles (red line).

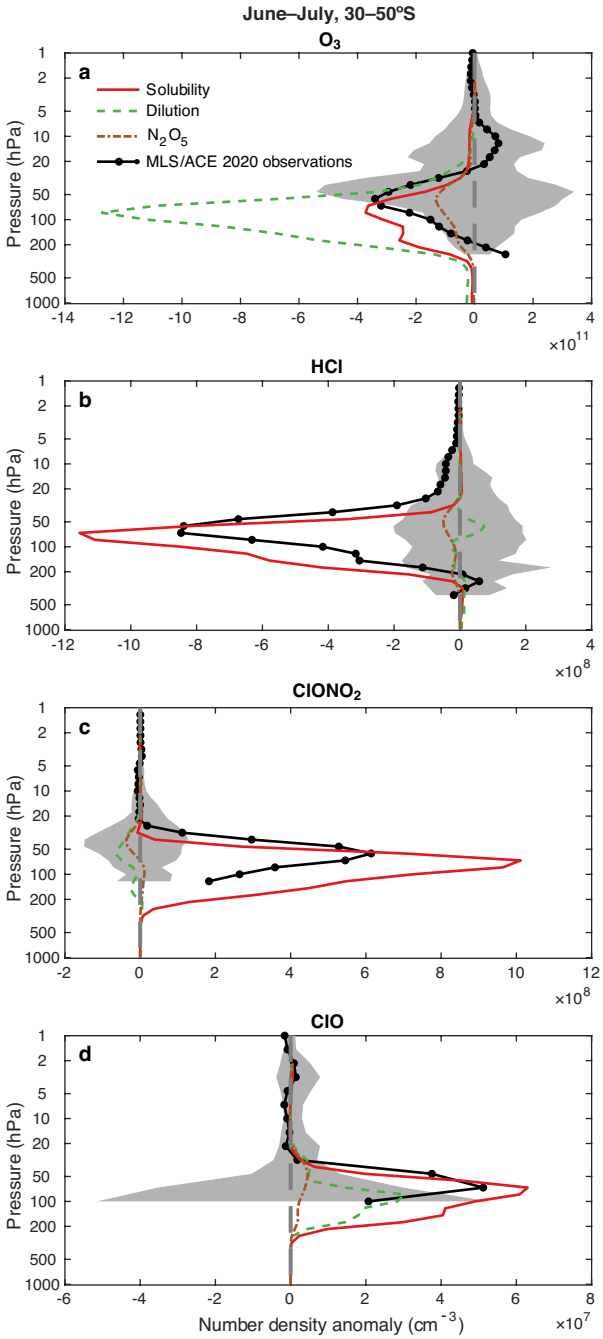

761

762 Fig. 3. **Observed and modelled vertical profile anomalies in chemical species from 30-**
763 **50°S in June-July, 2020.** Gray shaded regions show the ranges of 24-hour averaged
764 satellite data anomalies relative to the climatologies of satellite observations prior to
765 2020 (daily O_3 and ClO from MLS and HCl and monthly $ClONO_2$ from ACE, with coverage
766 to low altitudes), while black lines show observed anomalies for 2020. Other colored
767 lines denote calculated anomalies relative to the modelled no organics control for three
768 model test cases: including only N_2O_5 hydrolysis on the aerosols (brown dashed line),
769 considering the added organic material as a dilution factor (green dashed line), and
770 considering the adopted solubility of HCl in organic particles (red line).

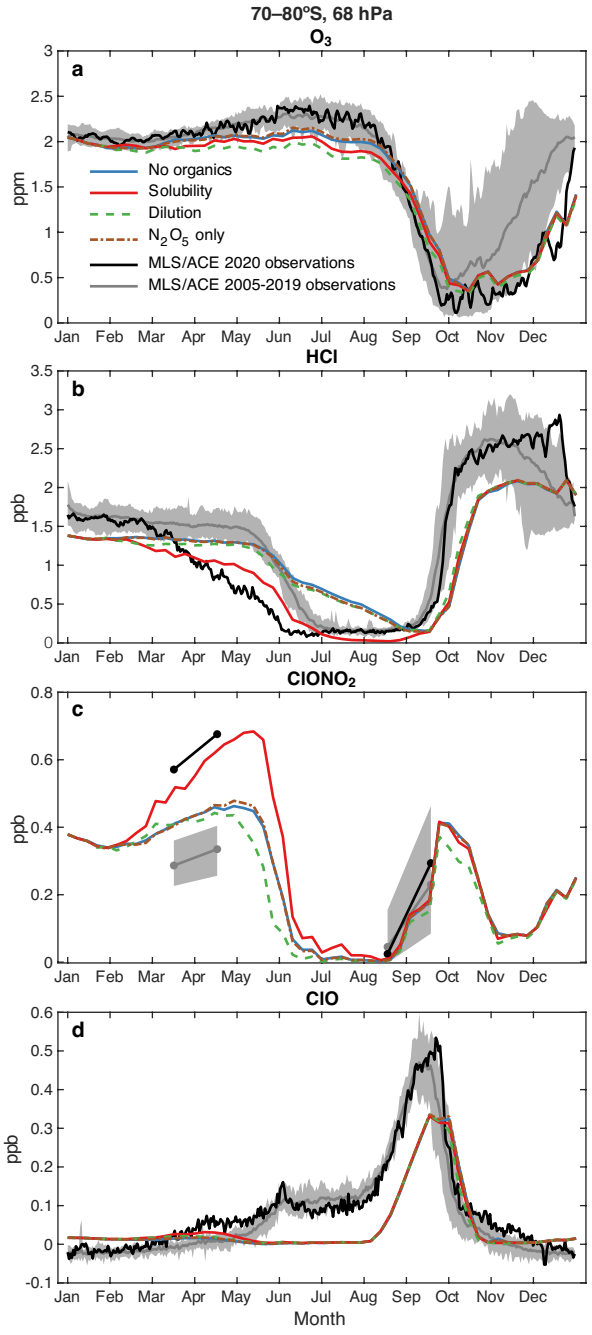

771

772 Fig. 4. **Observed and modelled mixing ratios of chemical species at 70-80°S, 68 hPa**.

773 Gray shaded regions show the ranges of 24-hour averaged satellite data (daily O_3, HCl,

774 and ClO from MLS, and monthly $ClONO_2$ from ACE) for prior years and the gray line

775 shows their averages, while black lines show observations for 2020. Other colored lines

776 show model calculated abundances for the no organics control run and for three model

777 test cases: including only N_2O_5 hydrolysis on the aerosols (brown dashed line),

778 considering the added organic material as a dilution factor (green dashed line), and

779 considering the adopted solubility of HCl in organic acid particles (red line).

780 Extended Data Figures

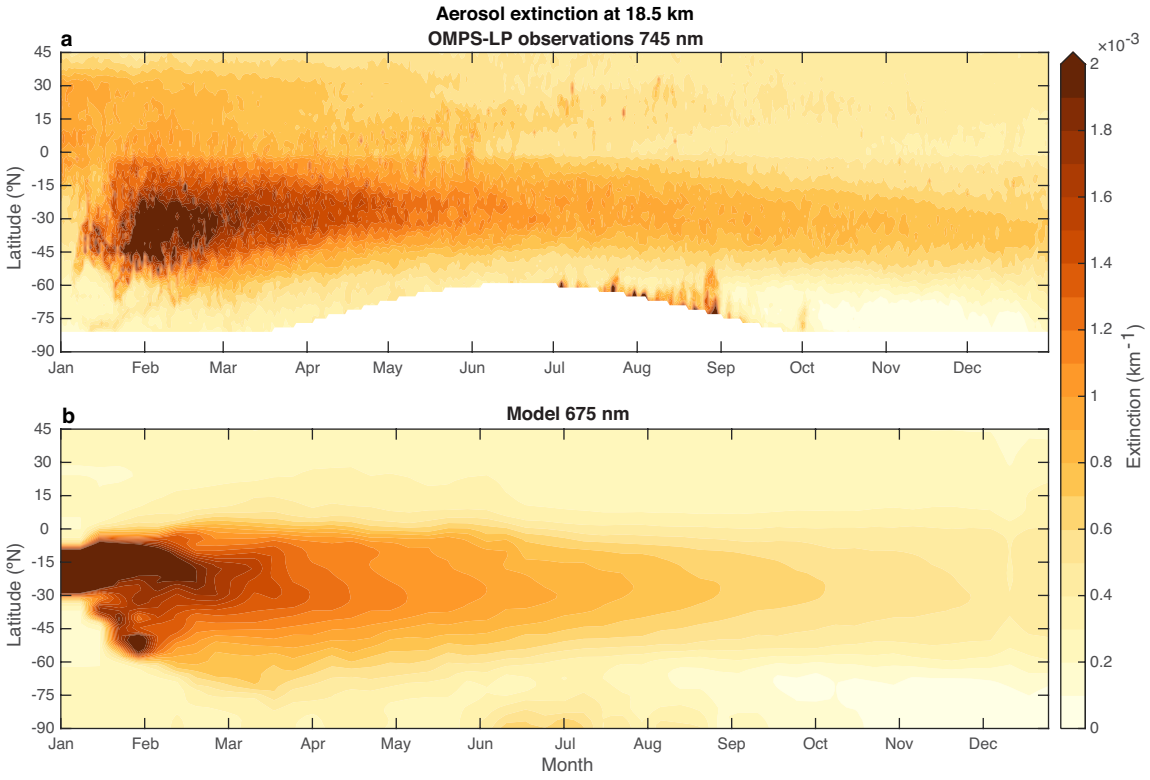

781

782

783 Extended Data Fig. 1. **Modelled (a) and observed (b) aerosol extinction at 18.5 km.**

784 The time evolution of aerosol extinction (km^{-1}) is shown at 18.5 km in the model (for 675

785 nm) and for OMPS observations (for 745 nm) in 2020.

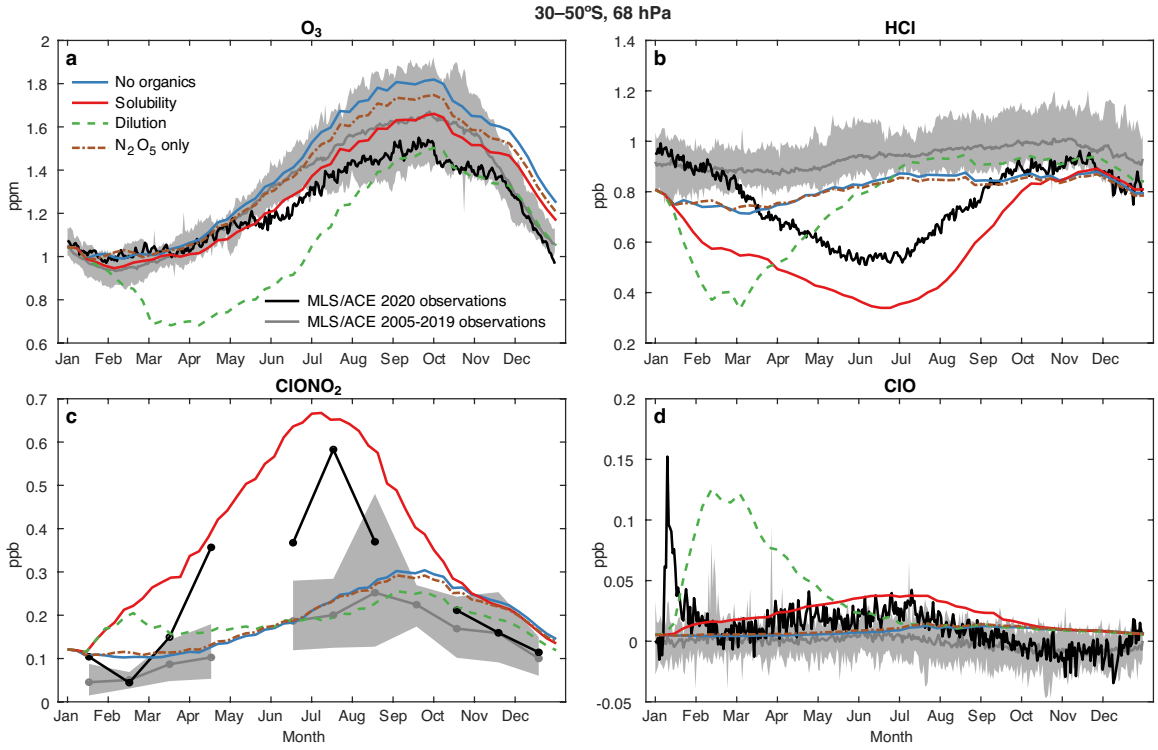

786

787

788 Extended Data Fig. 2. **Observed and modelled 2020 absolute abundances for chemical**

789 **species from 30-50°S at 68 hPa.** Gray shaded regions show the ranges of 24-hour

790 averaged satellite data from the climatologies of satellite observations (in mixing ratio

791 units) prior to 2020 (daily O_3, HCl, and ClO from MLS, and monthly $ClONO_2$ from ACE)

792 and the gray line shows their averages, while black lines show the observed values for

793 2020. Other colored lines show model calculated abundances for the no organics

794 control run (blue line) and for three model test cases: including only N_2O_5 hydrolysis on

795 the aerosols (brown dashed line), considering the added organic material as a dilution

796 factor (green dashed line), and considering the adopted solubility of HCl in organic acid

797 particles (red line). Corresponding anomalies are shown in Fig. 2.

798

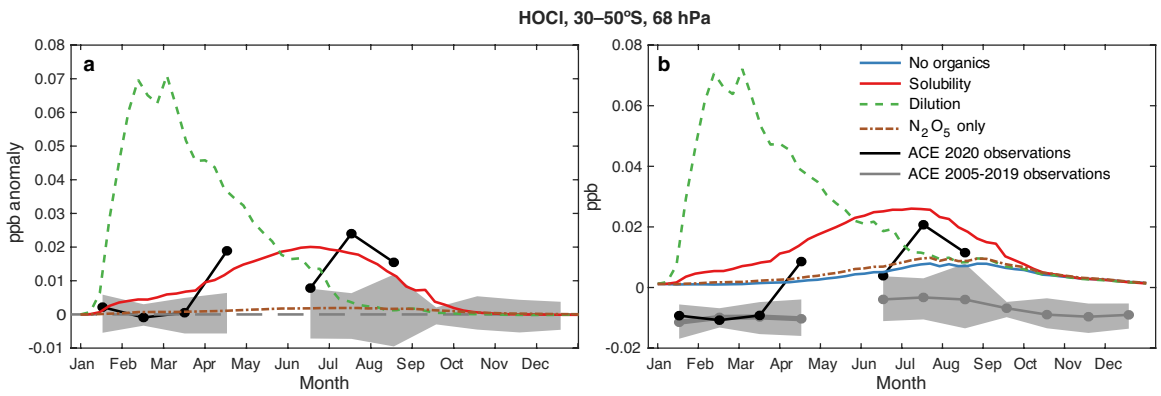

799

800 Extended Data Fig. 3. **Observed and modelled monthly averaged anomalies (a) and**
801 **mixing ratios (b) for HOCl (from ACE) for 30-50°S at 68 hPa.** Gray shaded regions show
802 the ranges of 24-hour averaged satellite data from the climatology prior to 2020, while
803 black lines show the observed values for 2020. Other colored lines show calculated
804 values for 2020 for the no organics control run (blue line) and for three model test
805 cases: including only N_2O_5 hydrolysis on the aerosols (brown dashed line), considering
806 the added organic material as a dilution factor (green dashed line), and considering the
807 adopted solubility of HCl in organic acid particles (red line).

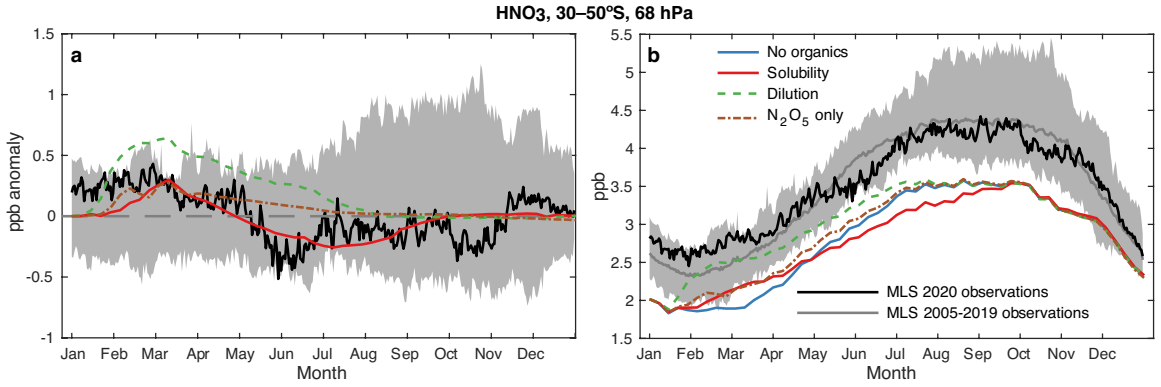

808

809 Extended Data Fig. 4. **Observed and modelled anomalies (a) and mixing ratios (b) for**
810 **HNO_3 (from MLS) for 30-50°S at 68 hPa.** Gray shaded regions show the ranges of 24-
811 hour daily averaged satellite data from the climatology prior to 2020, while black lines

812 show the observed values for 2020. Other colored lines show calculated values for
813 2020 for the no organics control run (blue line) and for three model test cases: including
814 only N_2O_5 hydrolysis on the aerosols (brown dashed line), considering the added organic
815 material as a dilution factor (green dashed line), and considering the adopted solubility
816 of HCl in organic acid particles (red line).

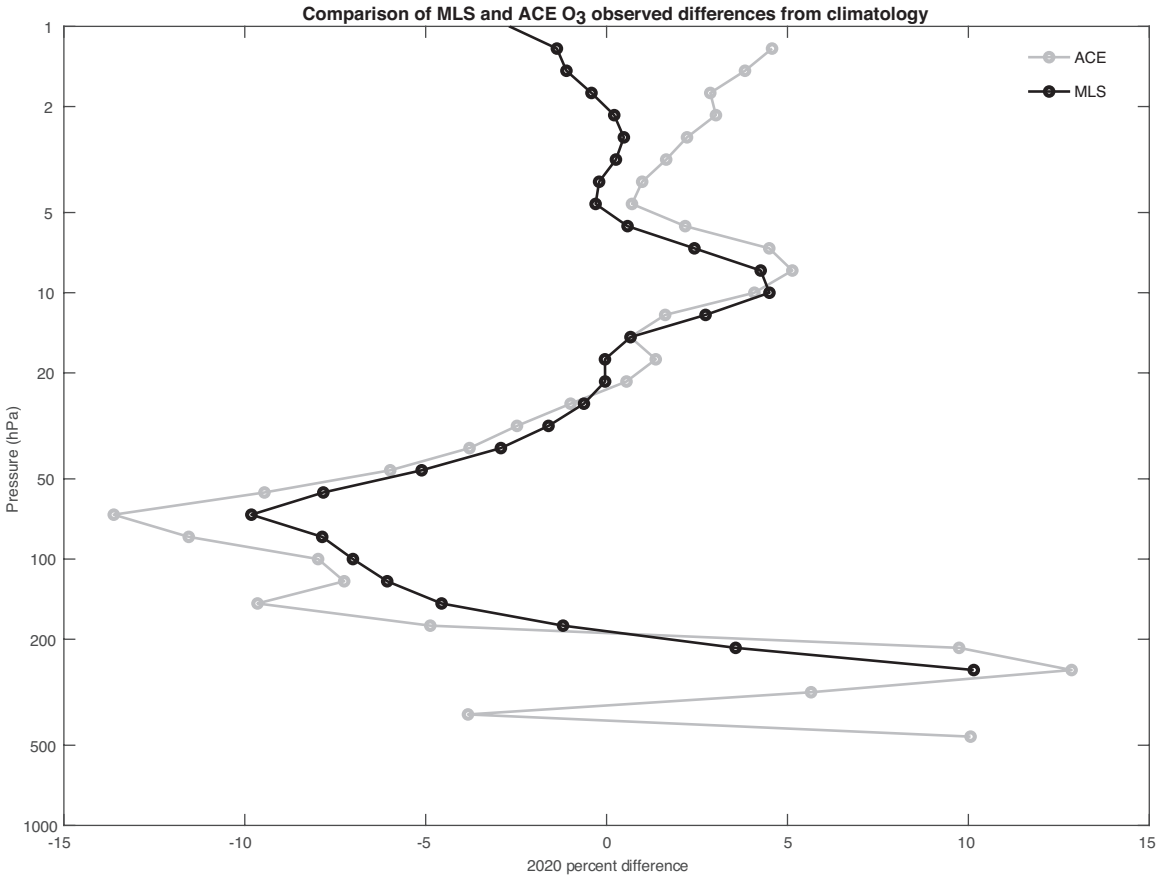

817

818 Extended Data Fig. 5. **Percent ozone anomalies for 30-50°S on coincident days of**
819 **measurement for ACE and MLS during June-July 2020, relative to their respective**
820 **climatologies.**

821

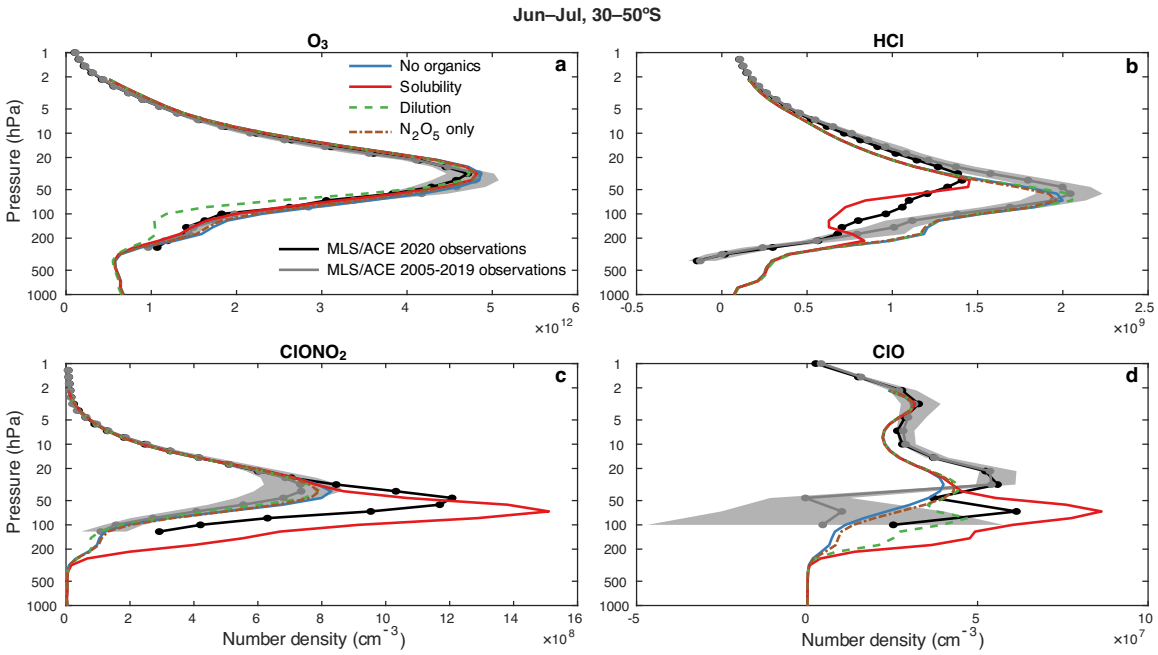

822

823 Extended Data Fig. 6. **Observed and modelled vertical profile absolute abundances for**

824 **chemical species from 30-50°S in June-July of 2020.** Gray shaded regions show the

825 ranges of 24-hour averaged satellite anomalies (in number density units) in years prior

826 to 2020 (daily O_3 and ClO from MLS and monthly HCl and $ClONO_2$ from ACE) and the

827 gray line shows their averages, while black lines show observed abundances for 2020.

828 Other colored lines show calculated values for 2020 for the no organics control run (blue

829 line) and for three model test cases: including only N_2O_5 hydrolysis on the aerosols

830 (brown dashed line), considering the added organic material as a dilution factor (green

831 dashed line), and considering the adopted solubility of HCl in organic acid particles (red

832 line). Corresponding anomalies are shown in Fig. 3.

833

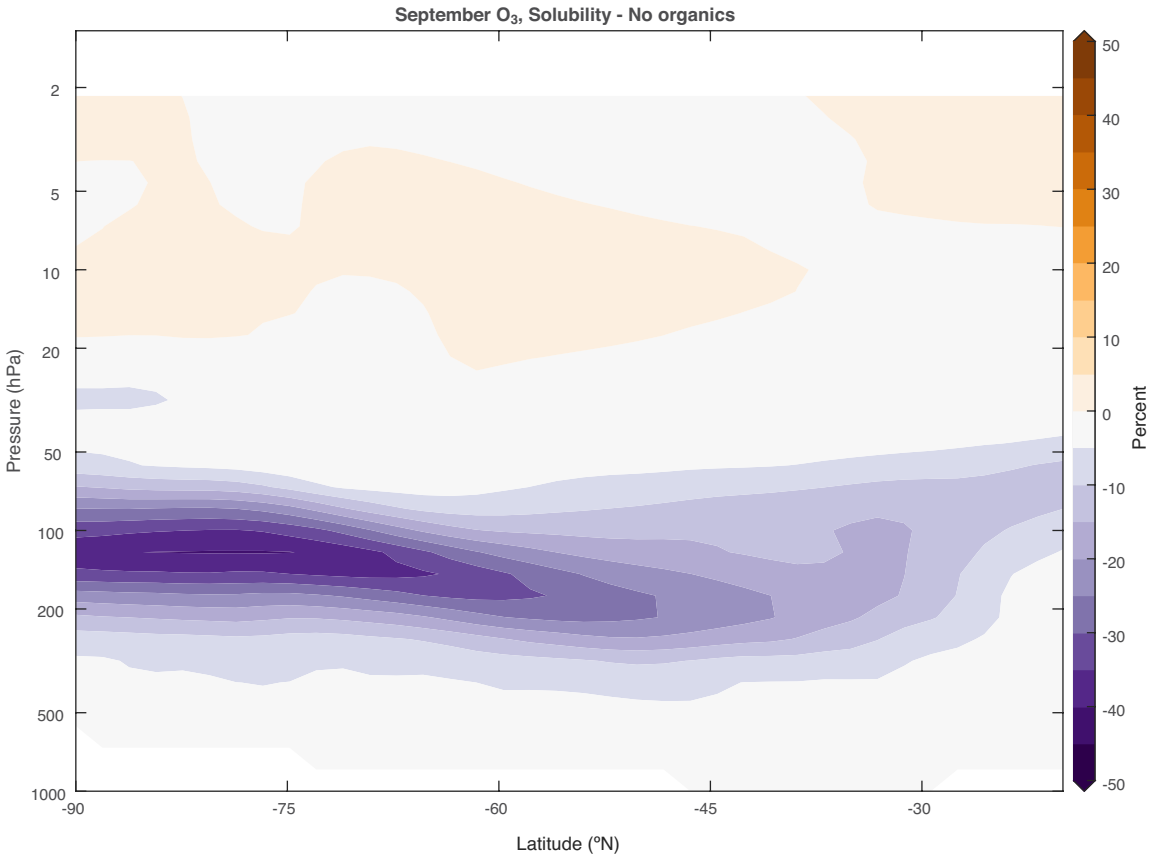

834

835 Extended Data Fig. 7. **Distribution of calculated ozone loss in September, 2020.**

836 Percentage change in model-calculated ozone as a function of latitude and height for

837 the oxidized organics solubility model case is shown, as compared to the no organics

838 control run.

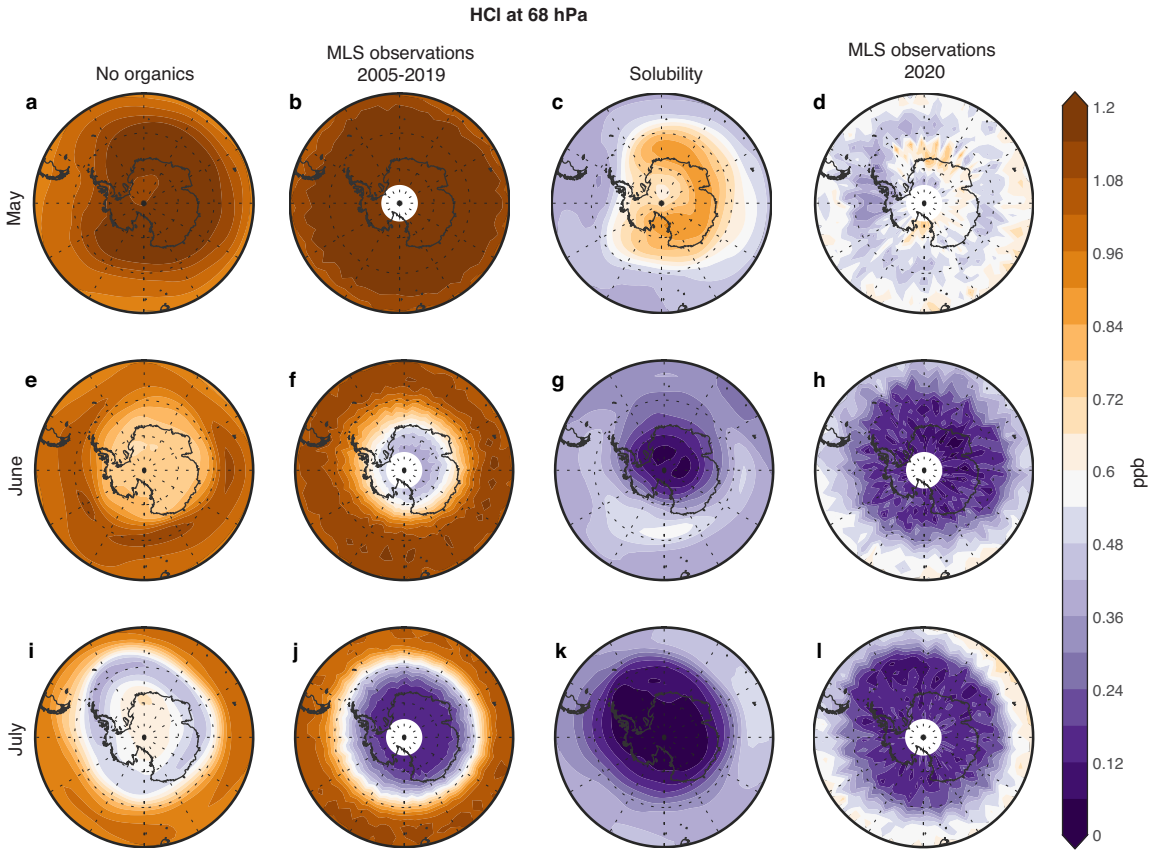

839

840 Extended Data Fig. 8. **Contour maps of monthly mean HCl abundances (ppbv) at 68**

841 **hPa for observations and models.** The modeled no organics control case is shown (left

842 column), along with MLS-measured climatological average from 2005-2019 (second

843 from left), modeled oxidized organics solubility case (second from right) and MLS

844 measurements for 2020 (right).

845

846

847

848